HHS Public Access

Author manuscript

J Orthop Res. Author manuscript; available in PMC 2024 May 01.

Published in final edited form as:

J Orthop Res. 2023 May ; 41(5): 1040–1048. doi:10.1002/jor.25443.

High-energy open-fracture model with initial experience of fluorescence-guided bone perfusion assessment

Valentin V. Demidov, Ph.D.[1,2], **Megan A. Clark**[3], **Samuel S. Streeter**[3], **J. Scott Sottosanti**[2], **I. Leah Gitajn, M.D.**[1], **Jonathan Thomas Elliott, Ph.D.**[1,2,3]

[1]Department of Orthopaedics, Dartmouth-Hitchcock Medical Centre, Lebanon, NH

[2]Geisel School of Medicine, Dartmouth College, Hanover, NH

[3]Thayer School of Engineering, Dartmouth College, Hanover, NH

Abstract

High-energy orthopaedic injuries cause severe damage to soft tissues and are prone to infection and healing complications, making them a challenge to manage. Further research is facilitated by a clinically translatable animal model with commensurate fracture severity and soft-tissue damage, allowing evaluation of novel treatment options and techniques. Here we report a reproducible, robust, and clinically relevant animal model of high-energy trauma with extensive soft-tissue damage, based on compressed air-driven membrane rupture as the blast wave source. As proof-of-principle showing the reproducibility of the injury, we evaluate changes in tissue and bone perfusion for a range of different tibia fracture severities, using dynamic contrast-enhanced fluorescence imaging and micro-computed tomography. We demonstrate that fluorescence tracer temporal profiles for skin, femoral vein, fractured bone and paw reflect the increasing impact of more powerful blasts causing a range of Gustilo grade I - III injuries. The maximum fluorescence intensity of distal tibial bone following 0.1 mg/kg intravenous indocyanine green injection decreased by 35% ($p < 0.01$), 75% ($p < 0.001$), and 87% ($p < 0.001$), following grade I, II, and III injuries, respectively, compared to uninjured bone. Other kinetic parameters of bone and soft tissue perfusion extracted from series of fluorescence images for each animal also showed an association with severity of trauma. In addition, the time-intensity profile of fluorescence showed marked differences in wash-in and wash-out patterns for different injury severities and anatomical locations. This reliable and realistic high-energy trauma model opens new research avenues to better understand infection and treatment strategies.

Level of Evidence: Level III; Case-control

Corresponding Author: Valentin V. Demidov, Ph.D., Postdoctoral Research Fellow, Dept of Orthopaedics, Dartmouth-Hitchcock Medical Center, Clinical Research Associate, Geisel School of Medicine, Dartmouth College, 750E Borwell Research, 1 Medical Center Drive, Lebanon, NH 03766, USA, Tel: +1 (603) 650 0805, valentin.demidov@dartmouth.edu.

Author Contributions Statement: VVD, MAC, SSS, ILG and JTE made substantial contributions to research design, or the acquisition, analysis or interpretation of data. All authors contributed to drafting the paper or revising it critically. All authors have read and approved the final submitted manuscript.

Conflict of interest and source of funding: The authors declare no potential conflicts of interest with respect to the research, authorship, and/or publication of this article. This research was funded by National Institutes of Health (R00CA190890) and internal funding from the Department of Orthopaedic Surgery at Dartmouth-Hitchcock Medical Center.

Institutional review board approval: Ethical approval to report this study was obtained from the Dartmouth Institutional Animal Care and Use Committee (protocol 2267)

Keywords

High-energy trauma; tibia fracture; fluorescence-guided surgery; optical imaging; computed tomography; dynamic contrast-enhanced fluorescence imaging

INTRODUCTION

High-energy tibia fractures are associated with significant soft-tissue damage and periosteal stripping of bone and are at high risk for infection and healing complications [1]. These injuries result from forces commuted during the impact, severely damaging skin and connective tissues, severing tendons and major blood vessels, and degloving or stripping periosteal tissues that surround and supply the bone with blood and nutrients. Management of these injuries can be challenging, with patients at risk for adverse outcomes. Tibia fractures represent ~40% of all long-bone fractures in adults [2] and one-third of these patients to require unplanned reoperation, often with worse outcomes. Five percent of patients ultimately undergo amputations [3]. These high rates of surgical site infection and complication suggest that there is a lack of understanding regarding modifiable risk factors that may influence the treatment outcome. Further studies with structured protocols involving realistic models of high-energy injury are needed to evaluate surgical and medical treatment options [4].

Most existing tibia trauma models (primarily in small animals) can cause an accurate fracture. However, in these models there is minimal soft-tissue injury with low to no complications. Highly reproducible transverse fracture model with a blunt guillotine driven by a dropped weight initially designed by Jackson et al. [5] and later optimized for rats [6] results in minimal tibia fracture comminution or angulation [7]. Three-point bending pliers [8] and their modifications [9, 10] create nondisplaced tibia fractures that demonstrate minimal edema and heal without such complications as delayed union, infection or soft tissue problems. Recently reported modification of a blunt guillotine model was able to achieve surrounding soft tissue injury and subsequent short-term complications by increasing the dropped weight elevation and mass [11]. Controlled impact, leading to a realistic multi-system trauma model, currently relies on artificial, three-point contact as the main trauma-incurring mechanism. In a realistic scenario, such as a motor vehicle hit of a pedestrian, forces act in a frontal plane causing bone fracture with skin, soft tissue and vascular-nervous injuries more similar to a result of a sudden blast [12].

To achieve a more realistic scenario of high-energy trauma resulting in a controlled open tibial fracture with severely damaged surrounding soft tissue, here we developed an approach utilizing the principle of compressed air-driven membrane rupture as the blast wave source [13]. After creating a table-top overpressure tube – a miniaturized version of a MacMillan blast device for lung [14] and brain [15] injury modelling – we determined whether it can accurately model high-energy trauma *in-vivo* in rats. The results presented here provide the first step in the creation of an injury-imaging platform for investigating how applied forces relate to tissue injury and perfusion. In this pilot study, we visualized fractured and adjacent bones with micro-resolution computed tomography (μCT) and

assessed perfusion of the bone and surrounding soft tissues with dynamic contrast enhanced fluorescence imaging (DCE-FI).

METHODS

High energy trauma model

The blast overpressure tube system was fabricated in-house from a polyvinyl chloride Schedule 40 (max working pressure = 1930 kPa) cylindrical tube (Charlotte Pipe, Charlotte, NC), separated using flanges into 2-ft long compression and 6-ft long expansion chambers by 3 to 5 mil (76 to 127 μm) thick polyethylene terephthalate (Mylar) membrane as shown schematically in Fig. 1A. An air compressor (Model C2002, Porter Cable Corp, Jackson, TN) with a built-in pressure regulator was connected to the compression chamber through a flexible hose and open-relief valve assembly. Diameter and wall thickness of the tube were chosen to stay below maximum pressures used in experiments according to the design and engineering documentation provided by the manufacturer [16]. The air compressor pressure regulator was set up to 145 psi (1000 kPa) with the relief valve *V1* protecting the system from overpressure. By opening the valve *V2*, the compression chamber was continuously filled with air until the Mylar membrane spontaneously ruptured (Fig. 1B) to create a shock wave propagating through the expansion chamber to hit the object at the open end. A custom animal holder (Fig. 1C) was designed using SolidWorks (Dassault Systemes SolidWorks Corp., Waltham, MA), 3D-printed using polylactic acid (Pruza Polymers, Prague, Czech Republic) and fixed on an adjustable platform (Fig. 1D) mounted on aluminum breadboards (MB1212 and MB2424, Thorlabs, Newton, NJ). Together with the optical imaging system shown schematically in Fig. 1E the entire experimental setup was compactly designed to fit on a regular lab benchtop (Fig. 1F).

A total of 18 Sprague-Dawley rats (6 cadavers and 12 live, Charles River, MA) aged 10–12 weeks and weighing 250 g to 350 g were used for animal experiments with all procedures being approved by the Dartmouth College Institutional Animal Care and Use Committee (IACUC protocol #2267). The overpressure blast tube setup was thoroughly calibrated with the 0–500 N/in^2 impact force meter and tested on cadavers before proceeding with *in-vivo* experiments. For the live animal experiments, rats were anesthetized with Isoflurane (5% for induction, 2% for maintenance) and given a perioperative dose of analgesia (Meloxicam, 1 mg/kg). Their legs (either left or right) were shaved, and the animals positioned in the holder before the tube output as demonstrated in Fig. 1G. Following Mylar membrane rupture, the blast overpressure wave exited the expansion chamber and hit the animal limb, fracturing the tibia and damaging the surrounding soft tissue. Animals were divided into four groups (n = 3 per group; 12 animals total): a control group and three groups subjected to single blasts with impact forces of 210, 320 and 430 N/in^2, (326, 496 and 667 kPa), respectively. These impact forces were experimentally chosen from cadaver tests.

Animal imaging

Following the blast, animals were positioned under the adjacently located optical imaging system (Fig. 1F) for assessment of fractured tibia bone, surrounding tissues and lower extremity blood perfusion changes compared to controls. For this, we employed our bone

perfusion-specific DCE-FI technique using indocyanine green (ICG) that was recently developed and tested on animals and humans [17–20]. ICG (0.1 mg/kg diluted in 200 μL of saline) was injected into each animal via a femoral vein catheter surgically installed by the animal supplier. Following the injection, optical image data were acquired using an in-house imaging system comprised of one scientific CMOS camera for RGB imaging (acA1920–155uc, Basler Inc., Exton, PA) and one for ICG imaging (Panda 4.2, PCO-Tech, Wilmington, DE). Fluorescence images were acquired at a frame rate of 5 Hz for a total of two minutes to capture ICG concentration rise and fall in the vasculature. Several color images were collected before and after fluorescent image acquisition. Both cameras were connected via a beam splitter to optical side ports of an OPMI-FC microscope (Carl Zeiss Inc., White Plains, NY) with an F-200mm objective lens and the rotating zoom-lens body adjusted to a 30cm working distance. Before animal experiments, using an ICG-equivalent resolution target (QUEL Imaging LLC, White River Junction, VT), the lateral resolution of the fluorescent imaging was measured to be 129 μm. Two optical filters (Chroma Technology Corp., Bellows Falls, VT) were installed before the PCO camera: a 780nm long pass filter (et780Ip) to reject the excitation light and a 770nm dichroic filter (t770Ipxr) to collect the ICG fluorescence emission. The high-energy trauma site was illuminated either with a white-light source for RGB image acquisition, or with a 740nm light-emitting diode for ICG image acquisition (Mightex LCS-0740, PhotonEdge Canada Inc. North York, ON, Canada).

After DCE-FI imaging, animals were euthanized and imaged with μCT. μCT scanning was performed using a commercial SpectrumCT (PerkinElmer, Waltham, MA). Scans settings were 50 kVp, 1 mA, 100 ms exposure per projection, 720 total projections, and 4-by-4 detector pixel binning. These settings resulted in a total scan time of ~4 min (~1.5 min for acquisition, ~2.5 min for filtered back projection reconstruction). The reconstructed volume was ~12 cm in diameter and ~3 cm in height with 150-μm voxels. Scan visualizations were achieved using 3D Slicer software [21].

Fluorescence data analysis

ICG image stacks were processed using ImageJ (National Institutes of Health, Bethesda, MD) and MATLAB (Mathworks, Natick, MA). Such biologically-relevant metrics as time-to-peak (TTP), ingress slope (IS), and maximum intensity (I_{max}) of ICG fluorescence temporal profiles [19] were used to characterize changes in perfusion at different sites near and in the location of high-energy trauma. To plot the fluorescence intensity profiles, regions of interest (ROIs) of equivalent size were applied to each background subtracted image in the stack. The size of each ROI was chosen to be 12x the resolution of the system, corresponding to a 23-by-23-pixel patch. Once applied, a threshold value of 0.25x the max pixel intensity in the ROI was applied to remove background noise and non-ROI specific information. Then, the mean intensity value within the ROI for each image in the sequence was calculated and plotted with respect to time. Initial fluctuations in signal before the characteristic slope were removed. Each trauma level case was normalized to the maximum value of the femoral vein ROI, for comparison, as the vein remained most consistent through trauma energy cases and had the highest intensity. I_{max} was defined as the maximum intensity value of the intensity profile, TTP was defined as the time from 2%

I_{max} to I_{max} and IS was defined as the slope from 25% I_{max} to 75% I_{max}. Perfusion maps for each case were then calculated by down sampling the images and calculating the value from the entire stack for each pixel in the image, with a color bar providing visualization of the change in these parameters with trauma level. Each parameter for each ROI was then averaged for comparison, and the standard deviation for each value was calculated from the ROI selected. Data is presented as mean value ± standard deviation and is analyzed for variance by ANOVA to evaluate the differences between groups by SPSS statistical tool (V22, IBM Corp, NY). Pairwise t-tests were conducted between baseline and other three groups for each parameter, and a Bonferoni correction was applied to account for multiple comparisons. $P < 0.05$ was considered statistically significant.

Injury assessment and categories

Based on the μCT images, DCE-FI data and clinical characters, the fracture and soft tissue injury types were evaluated by a senior orthopaedic surgeon (ILG) according to the Orthopaedic Trauma Association and Gustilo-Anderson classifications [22,23]. Fractures were divided into three categories: type I (open fracture with small poke hole, minimal soft tissue injury and periosteal stripping), type II (open fractures with moderate soft tissue injury), type IIIa/b (severe open fractures with extensive soft tissue injury, and periosteal stripping), and type IIIc (severe open fracture with extensive soft tissue injury, periosteal stripping and vascular injury leading to acute limb ischemia).

RESULTS

Mylar membranes of 3, 4 and 5 mil (76, 102 and 127 μm) thickness were used in the system with installed force meter to explore the range of membrane rapture pressures and impact forces created at the output of the expansion chamber. Linear dependence of impact force (Fi) on Mylar rapture pressure was measured with high repeatability (Fig. 2A), providing a useful relationship between Mylar thickness T_m and resulting impact force [$F_i = 2.32\ \mu m \cdot N^{-1} \cdot in^2 \times T_m$, $r^2 = 0.99$, $p < 0.001$]. After blast tube calibration and tests on cadavers (Fig. 2B), anesthetized rats were used for *in-vivo* experiments.

Various peak overpressure blasts were tested to determine which pressures caused the desired severity of injury, while still being salvageable, so that the animal could be repaired surgically and recovered humanely with the use of a multidrug analgesia plan. For this, fractured and surrounding bones were 3D-rendered with μCT and soft-tissue and bone perfusion was evaluated with fluorescence-guided imaging. Fig. 2C shows inferior μCT projections (Fig. 2C, **top row**) after blasts with 210, 320 and 430 N/in^2 impact forces. Overpressure tube design allowed for precise direction of the blast into the tibia-fibula area only, not affecting other skeletal bones and keeping knees and ankles intact. Fig. 2C (**bottom row**) presents white-light images obtained with the RGB camera and enlarged μCT projections: a simple transverse fracture with the minimum impact force of 210 N/in^2, a moderate (320 N/in^2) fracture and a severe (430 N/in^2) fracture.

After each blast, animals were transferred to a nearby imaging system for DCE-FI imaging. Together with DCE-FI, visual observations and μCT image analysis facilitated injury level classification summarized in Table 1. The RGB images in Fig. 3 (**left column**) show the

different trauma level cases: control (bare skin), 0 N/in^2 (exposed intact bone), 210 N/in^2, 320 N/in^2 and 430 N/in^2. For imaging bone and surrounding tissue perfusion, full skin incisions were made in (b) and (c) cases, partial skin incisions (between lacerations) were made in (d) cases and no incisions in severe impact force (e) cases. The background subtracted, maximum fluorescence intensity images are shown in Fig. 3 (**central column**), demonstrating the system's ability to track ICG fluorescence through the entire leg under different trauma conditions. ROIs were chosen based on their relevance to fracture evaluation. The fluorescence intensity profiles for each energy level at each ROI are shown in Fig. 3 (**right column**). The profiles demonstrate changes in shape, or lack thereof, based on each ROI. The vein (blue square) and skin (yellow square) regions offer insight into the perfusion of the proximal side of the fracture site, where perfusion should not be significantly affected with the impact force. Indeed, in all five cases shown in the figure, signals from vein and skin demonstrate respectively similar behavior. In contrast, the paw ROI offers insight into the perfusion of the distal side of the fracture site and should be affected by fracture energy. ICG intensity profiles show slower dye accumulation in the lower extremity with high energy impact force, which indicates major supplying vasculature damage. For direct bone perfusion evaluation before and after fracture, ROIs were chosen on either end of the bone. The higher the impact force, the more distinct the proximal and distal bone intensity profiles are, reflecting the higher degree of injury to the tibia. Following grade I, II, and III injuries, peak fluorescence intensity of the distal side notably decreased by 35% ($p < 0.01$), 75% ($p < 0.001$), and 87% ($p < 0.001$), respectively, compared to uninjured bone.

Visual and numerical classification of changes in ICG fluorescence intensity profile shape can be seen in Fig. 4, demonstrating the dependence of the characteristic parameters of profiles, and hence, the tissue perfusion on impact force. TTP values in the *bone* and *paw* ROIs (Fig. 4A) grow with increasing force, while TTP of the *skin* does not demonstrate force-dependent changes. Both the proximal and distal bones TTPs increased from 57±19 s and 64±10 s (intact bone) to >120 s (non-zero impact forces) ($p<0.05$). Similarly, Fig. 4B shows the IS of the bone and paw ROIs decreasing with increasing impact force. The IS of the paw ROI, proximal bone ROI, and distal bone ROI for the 0 N/in^2 case were calculated to be 0.15±0.01 units/s, 0.25±0.04 units/s and 0.17±0.01 units/s, respectively; rapidly decreasing in bone to 0.01–0.07 units/sec levels for 210–430 N/in^2 cases proportionally to applied force. Bone ROI I_{max} intensity gradually decreased, depending on the applied force, for both the proximal and distal aspects, changing from 0.57±0.04 units/s and 0.47±0.04 units/s (0 N/in^2) to 0.18±0.03 units/s and 0.06±0.003 units/s (430 N/in^2) ($p < 0.001$).

DISCUSSION

Animal fracture models have been extensively used for decades in preclinical orthopaedics research [24,25] with rats being the most popular [26], to establish strategies to further understand the physiology of bone healing and to improve treatment outcomes. Traditionally, the physical impact for orthopaedic trauma models was generated using a falling weight or bending pliers [5,8]. With the advent of blast overpressure models in the study of traumatic brain injury and other blast-related trauma, these impact mechanisms have now been applied to orthopaedic trauma research. As severely damaged soft tissues in the setting of displaced tibia fracture are prone to infection and healing complications,

a growing area of research is in the development of methods to assess and treat wounds in an effort to reduce risk of infection and other complication. One such approach has been developing objective or quantitative methods to assess bone and soft tissue viability which can be used to guide surgical debridement. While fluorescence-guided surgery has been used extensively in other types of surgeries to visualize flow, tissue perfusion, and molecular expression, only recently have there been attempts to use quantitative methods to guide *orthopaedic* surgery [17–19,27–29]. As presented here, combination of a clinically relevant animal model of high energy trauma with the fluorescence imaging provides a unique research tool for extraction of biologically relevant parameters of injured tissues.

The straightforward implementation of fluorescence imaging would be to inject ICG to obtain a single time-point intensity image (*e.g.*, as shown in Fig. 3, middle column) as an estimate of perfusion [30]. However, in polytrauma patients with diverse comorbidities and circulatory health, a single time point image will be influenced by the patient-specific arterial input function, timing, injection method and other parameters [18]. Thus, here a more advanced and sophisticated method of kinetic analysis was evaluated to extract perfusion metrics of affected areas. Supported by μCT images of fractured bones (examples shown in Fig. 2) characterizing fracture location and severity, we demonstrate how ICG kinetics reveal soft tissue and bone damage perfusion changes with increasing impact force. ICG intensity temporal profiles plotted in Figure 3 for skin, femoral vein, fractured bone and paw ROIs reflect the increasing impact of the applied force on perfusion after more powerful blasts. The extracted kinetic parameters from series of ICG fluorescence images of soft tissues and bone perfusion assessment shown in Fig.4 correlate well with trauma classification grades (Table 1) which potentially may be used for fast diagnosis in the field by inexperienced surgeons. Detailed investigation of this correlation with more animals for comparison, supported by adequate modeling, may lead to the creation of a diagnostic tool for timely suggestion or correction of trauma treatment strategies. While the characterization of not only animals, but also human responses of fluorescence imaging to orthopaedic trauma is relatively nascent, our results in this limited series of animals are consistent with how these fractures present in clinical practice [31].

Advantages of our approach are a low equipment cost, fast speed of trauma creation, and compatibility with fracture fixation experimentation as well as potential for inoculation with bacteria. The latter two are critical for advancing the field of orthopaedic trauma management, as high-energy orthopaedic injuries with severely damaged vasculature and displaced fractures are prone to infection and healing complications. The proposed clinically translatable animal model may thus be used not only for initial post-trauma perfusion level assessment but potentially for longitudinal evaluation of treatment options and anti-bacterial strategies to improve outcomes.

CONCLUSION

In this work, we presented a clinically relevant animal model of high energy trauma at a range of Gustilo grade injuries with the predictive value of different parameters obtained by dynamic contrast enhanced fluorescence imaging. The extracted kinetic parameters correlate well with trauma classification grades; in clinical studies undertaken by our team, we

explore the use of these ICG related parameters as an assessment tool. Future work will investigate this correlation in detail with more animals for comparison and evaluate the level of improvement in outcomes of debridement guided by extracted kinetic parameters with respect to injury treatment and prevention of infection.

Acknowledgements

This study was funded by the National Institutes of Health (R00CA19089) and the Department of Orthopaedics at Dartmouth-Hitchcock Medical Centre. Authors would like to thank Dr. P.M. Werth for advising on appropriate statistical analysis of experimental data.

REFERENCES

1. Tejwani NC, Hak DJ, Finkemeier CG, Wolinsky PR. High-energy proximal tibial fractures: treatment options and decision making. Instr. Course Lect 2006 Jan;55:367–379. [PubMed: 16958472]
2. Court-Brown CM, Caesar B. Epidemiology of adult fractures: A review. Injury 2006 Aug;37(8):691–7. doi: 10.1016/j.injury.2006.04.130. [PubMed: 16814787]
3. Henkelmann R, Frosch KH, Glaab R, Lill H, Schoepp C, Seybold D et al. Committee TRAUMA of the AGA-Society for Arthroscopy and Joint Surgery. Infection following fractures of the proximal tibia - a systematic review of incidence and outcome. BMC Musculoskelet. Disord. 2017 Nov 21;18(1):481. doi: 10.1186/s12891-017-1847-z. [PubMed: 29162084]
4. Liu Y, Liu J, Yushan M, Liu Z, Zhang T, Ma H et al. Management of high-energy tibial shaft fractures using the hexapod circular external fixator. BMC Surg. 2021;21(95): 1–9. doi.org/10.1186/s12893-021-01106-5 [PubMed: 33388031]
5. Jackson RW, Reed CA, Israel JA, Abou-Keer FK, Garside H. Production of a standard experimental fracture. Can J Surg. 1970 Oct;13(4):415–420. [PubMed: 5506099]
6. Bonnarens F, Einhorn TA. Production of a standard closed fracture in laboratory animal bone. J. Orthop. Res. 1984;2(1):97–101. doi: 10.1002/jor.1100020115. [PubMed: 6491805]
7. An Y, Friedman RJ, Parent T, Draughn RA. Production of a standard closed fracture in the rat tibia. J. Orthop. Trauma 1994;8(2):111–5. doi: 10.1097/00005131-199404000-00006. [PubMed: 8207566]
8. Greiff J A method for the production of an undisplaced reproducible tibial fracture in the rat. Injury. 1978 May;9(4):278–81. doi: 10.1016/s0020-1383(77)80044-2. [PubMed: 649188]
9. Otto TE, Patka P, Haarman HJ. Closed fracture healing: a rat model. Eur Surg Res. 1995;27(4):277–84. doi: 10.1159/000129410. [PubMed: 7649215]
10. Handool KO, Ibrahim SM, Kaka U, Omar MA, Abu J, Yusoff MSM et al. Optimization of a closed rat tibial fracture model. J. Exp. Orthop 2018 May 2;5(1):13. doi: 10.1186/s40634-018-0128-6. [PubMed: 29721763]
11. Shi E, Chen G, Qin B, Yang Y, Fang J, Li L et al. A novel rat model of tibial fracture for trauma researches: a combination of different types of fractures and soft tissue injuries. J. Orthop. Surg. Res. 2019;14:333. doi: 10.1186/s13018-019-1386-4 [PubMed: 31651336]
12. Otte D, Haasper C. Characteristics on fractures of tibia and fibula in car impacts to pedestrians and bicyclists - influences of car bumper height and shape. Annu. Proc. Assoc. Adv. Automot. Med. 2007;51:63–79. [PubMed: 18184485]
13. Clemedson CJ. An experimental study on air blast injuries. Acta Physiol. Scand, Almqvist & Wiksell. 18, Suppl. 61 (1949).
14. Chavko M, Prusaczyk WK, McCarron RM. Lung injury and recovery after exposure to blast overpressure. J. Trauma. 2006 Oct;61(4):933–42. doi: 10.1097/01.ta.0000233742.75450.47. [PubMed: 17033565]
15. Mishra V, Skotak M, Schuetz H, Heller A, Haorah J, Chandra N et al. Primary blast causes mild, moderate, severe and lethal TBI with increasing blast overpressures: Experimental rat injury model. Sci. Rep. 2016; 6:26992. 10.1038/srep26992 [PubMed: 27270403]

16. Charlotte Pipe plastics technical and installation manual. 120 pages (2022), https://www.charlottepipe.com/Documents/PL_Tech_Man/Charlotte_Plastics_Tech_Manual.pdf

17. Elliott JT, Jiang S, Pogue BW, Gitajn IL. Bone-specific kinetic model to quantify periosteal and endosteal blood flow using indocyanine green in fluorescence guided orthopedic surgery. J. Biophotonics. 2019 Aug;12(8):e201800427. doi: 10.1002/jbio.201800427. [PubMed: 30963727]

18. Elliott JT, Addante RR, Slobegean GP, Jiang S, Henderson ER, Pogue BW et al. Intraoperative fluorescence perfusion assessment should be corrected by a measured subject-specific arterial input function. J. Biomed. Opt. 2020 Jun;25(6):1–14. doi: 10.1117/1.JBO.25.6.066002.

19. Gitajn IL, Elliott JT, Gunn JR, Ruiz AJ, Henderson ER, Pogue BW et al. Evaluation of bone perfusion during open orthopedic surgery using quantitative dynamic contrast-enhanced fluorescence imaging. Biomed. Opt. Express. 2020 Oct 19;11(11):6458–6469. doi: 10.1364/BOE.399587. [PubMed: 33282501]

20. Han X, Demidov V, Gitajn IL, Jiang S, Elliott JT. Intraoperative assessment of patient bone viability using texture analysis of dynamic contrast-enhanced fluorescence imaging. European Conferences on Biomedical Optics 2021;119190A. doi: 10.1117/12.2614457.

21. Fedorov A, Beichel R, Kalpathy-Cramer J, Finet J, Fillion-Robin JC, Pujol S et al. 3D Slicer as an image computing platform for the Quantitative Imaging Network. Magn. Reson. Imaging. 2012 Nov;30(9):1323–41. doi: 10.1016/j.mri.2012.05.001. [PubMed: 22770690]

22. Agel J, Evans AR, Marsh JL, Decoster TA, Lundy DW, Kellam JF et al. The OTA open fracture classification: a study of reliability and agreement. J. Orthop. Trauma. 2013 Jul;27(7):379–84; discussion 384–5. doi: 10.1097/BOT.0b013e3182820d31. [PubMed: 23287764]

23. Willmott H Trauma and orthopaedics at a glance. 1st Ed., Wiley Blackwell UK 2016, 128 p. ISBN: 978–1-118–80253-3.

24. Rhinelander FW, Phillips RS, Steel WM, Beer JC. Microangiography in bone healing. II. Displaced closed fractures. J. Bone Joint Surg. Am. 1968 Jun;50(4):643–662 passim. doi: 10.2106/00004623-196850040-00001. [PubMed: 5658552]

25. Chakkalakal DA, Strates BS, Mashoof AA, Garvin KL, Novak JR, Fritz ED et al. Repair of segmental bone defects in the rat: an experimental model of human fracture healing. Bone. 1999 Sep;25(3):321–332. doi: 10.1016/s8756-3282(99)00167-2. [PubMed: 10495136]

26. O'Loughlin PF, Morr S, Bogunovic L, Kim AD, Park B, Lane JM. Selection and development of preclinical models in fracture-healing research. J. Bone Joint Surg. Am. 2008 Feb;90 Suppl 1:79–84. doi: 10.2106/JBJS.G.01585. [PubMed: 18292361]

27. Han X, Demidov V, Wirth D, Byrd B, Davis SC, Gitajn IL et al. Validation of dynamic contrast-enhanced bone blood flow imaging technique with fluorescent microspheres. SPIE BiOS, Molecular-Guided Surgery 2022; 119430H. doi: 10.1117/12.2608228.

28. Han X, Demidov V, Wirth D, Byrd B, Davis SC, Gitajn IL et al. Initial experience of perfusion assessment in a rabbit model of orthopaedic trauma surgery using fluorescent microspheres and hyperspectral imaging cryomacrotome. SPIE Photonics Europe, Clinical Biophotonics 2022; 1214609. doi: 10.1117/12.2624185.

29. Han X, Demidov V, Vaze VS, Jiang S, Gitajn IL, Elliott JT. Spatial and temporal patterns in dynamic-contrast enhanced intraoperative fluorescence imaging enable classification of bone perfusion in patients undergoing leg amputation. Biomed. Opt. Exp. Jun 2022;13(6):3171–3186. doi: 10.1364/BOE.459497.

30. DSouza AV, Lin H, Henderson ER, Samkoe KS, Pogue BW. Review of fluorescence guided surgery systems: identification of key performance capabilities beyond indocyanine green imaging. J. Biomed. Opt. 2016 Aug 1;21(8):80901. doi: 10.1117/1.JBO.21.8.080901. [PubMed: 27533438]

31. Harris AM, Althausen PL, Kellam J, Bosse MJ, Castillo R; Lower Extremity Assessment Project (LEAP) Study Group. Complications following limb-threatening lower extremity trauma. J. Orthop. Trauma 2009 Jan;23(1):1–6. doi: 10.1097/BOT.0b013e31818e43dd. [PubMed: 19104297]

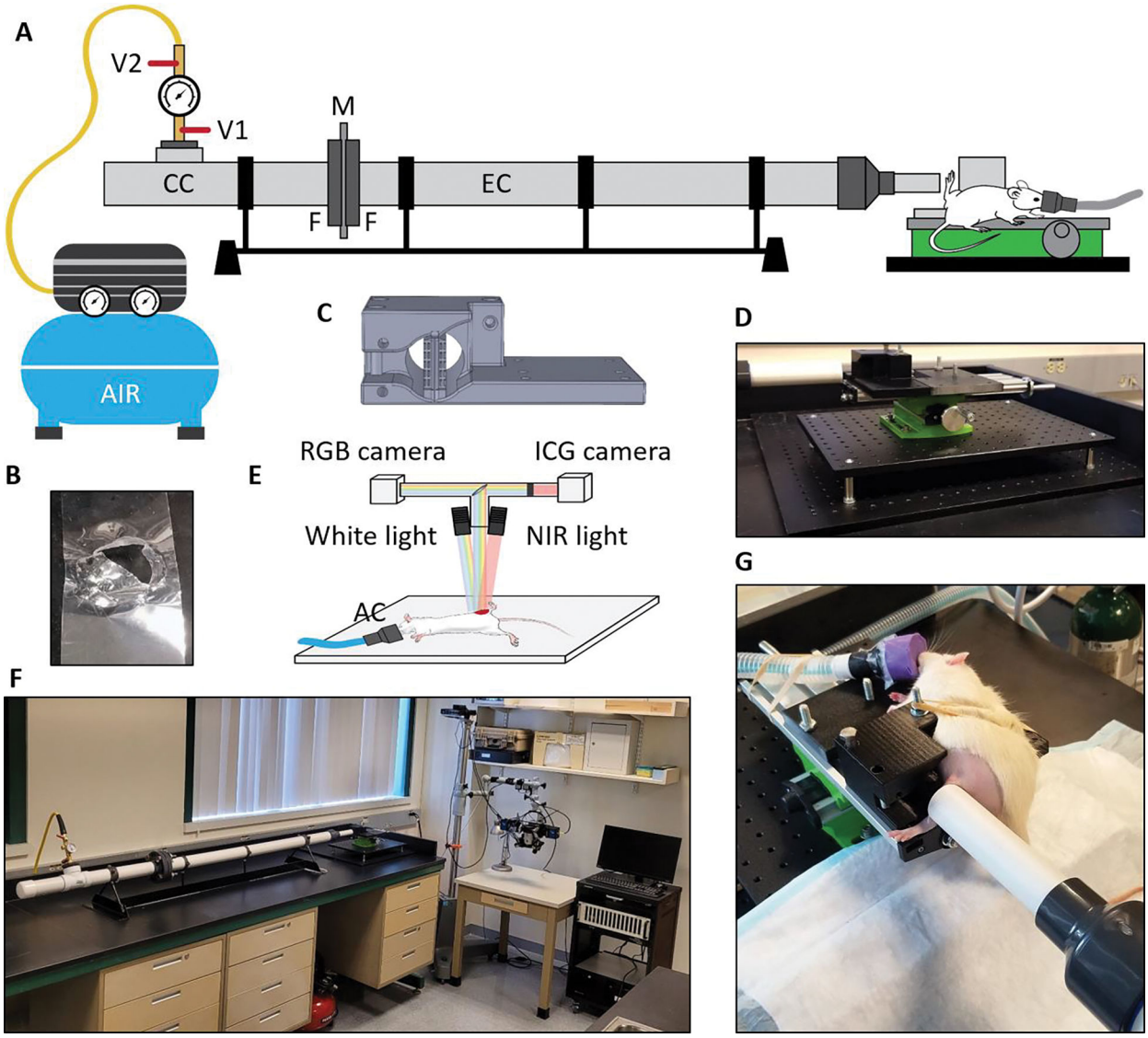

Figure 1.

High-energy trauma model. (**A**) Schematic of the blast overpressure tube system with the Mylar sheet and animal holder in place. V1 – relief valve, V2 – air valve, CC – compression chamber, M – Mylar membrane, F – flanges bolted together, EC – expansion chamber; (**B**) Ruptured 3mil Mylar sheet after blast; (**C**) 3D model of the animal holder; (**D**) Adjustable platform with installed animal holder; (**E**) Schematic of the imaging system, NIR – near infrared, AC – anesthesia cone; (**F**) Compact setup of blast overpressure tube and imaging system in the lab; (**G**) Anesthetized rat in the holder before a blast with the leg positioned freely close to the output end of the expansion chamber.

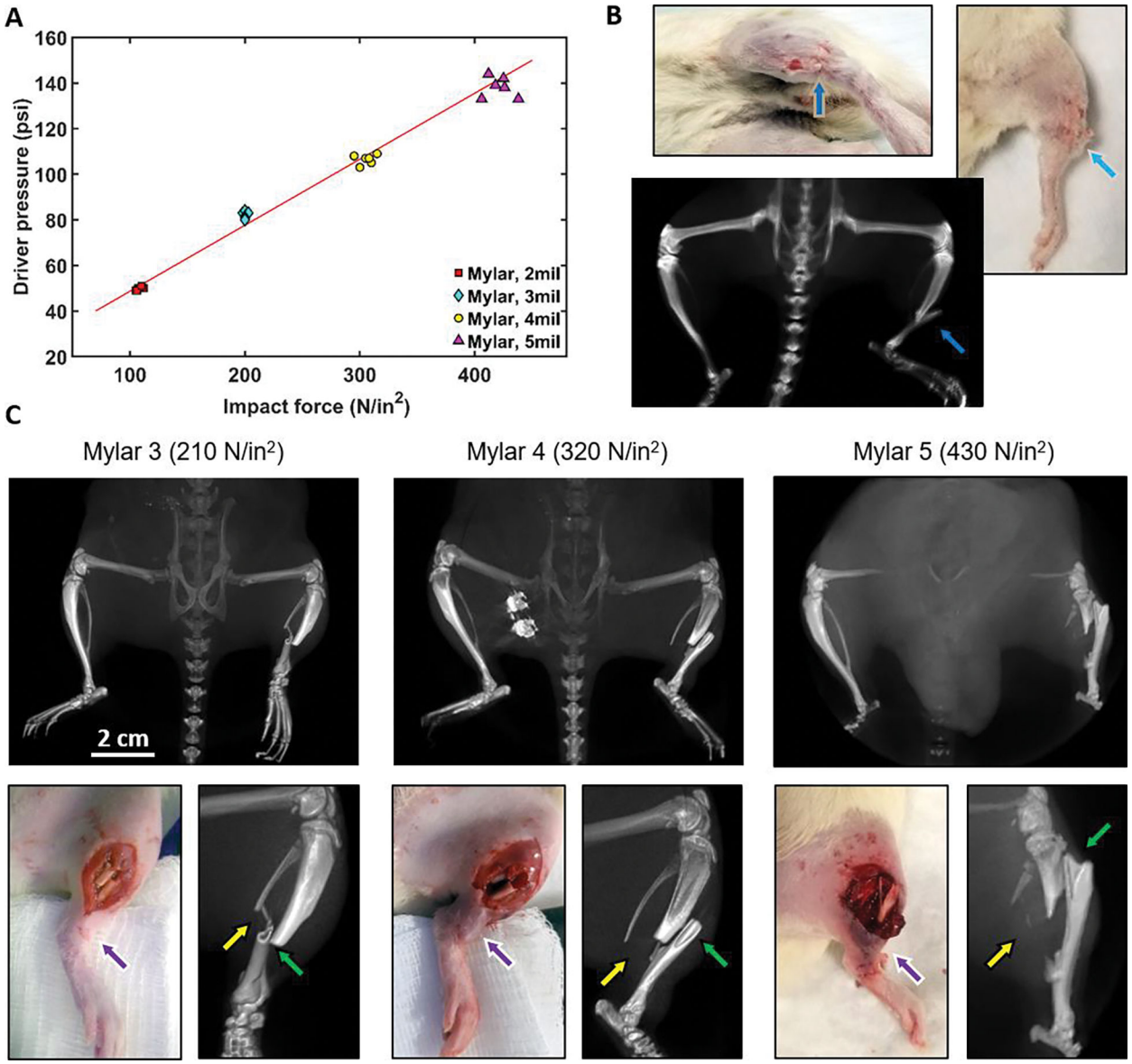

Figure 2.

Blast overpressure tube testing and experimentation. (**A**) Measurement of membrane rapture pressures and impact forces created at the output of the expansion chamber; **(B)** Cadaver testing: white-light photographs of a rat cadaver subjected to a high-energy blast (Mylar 3mil membrane) and corresponding projection of a 3D μCT scan of the injured area with blue arrows indicating the fracture location; (**C**) High-energy trauma modeling *in-vivo* with 210, 320 and 430 N/in^2 impact forces: μCT projections (top row), RGB images and enlarged μCT projections (bottom row) of injured areas. Green and yellow arrows indicate tibia and fibula fractures, respectively. Purple arrows indicate the increase in soft tissue damage with increasing impact force.

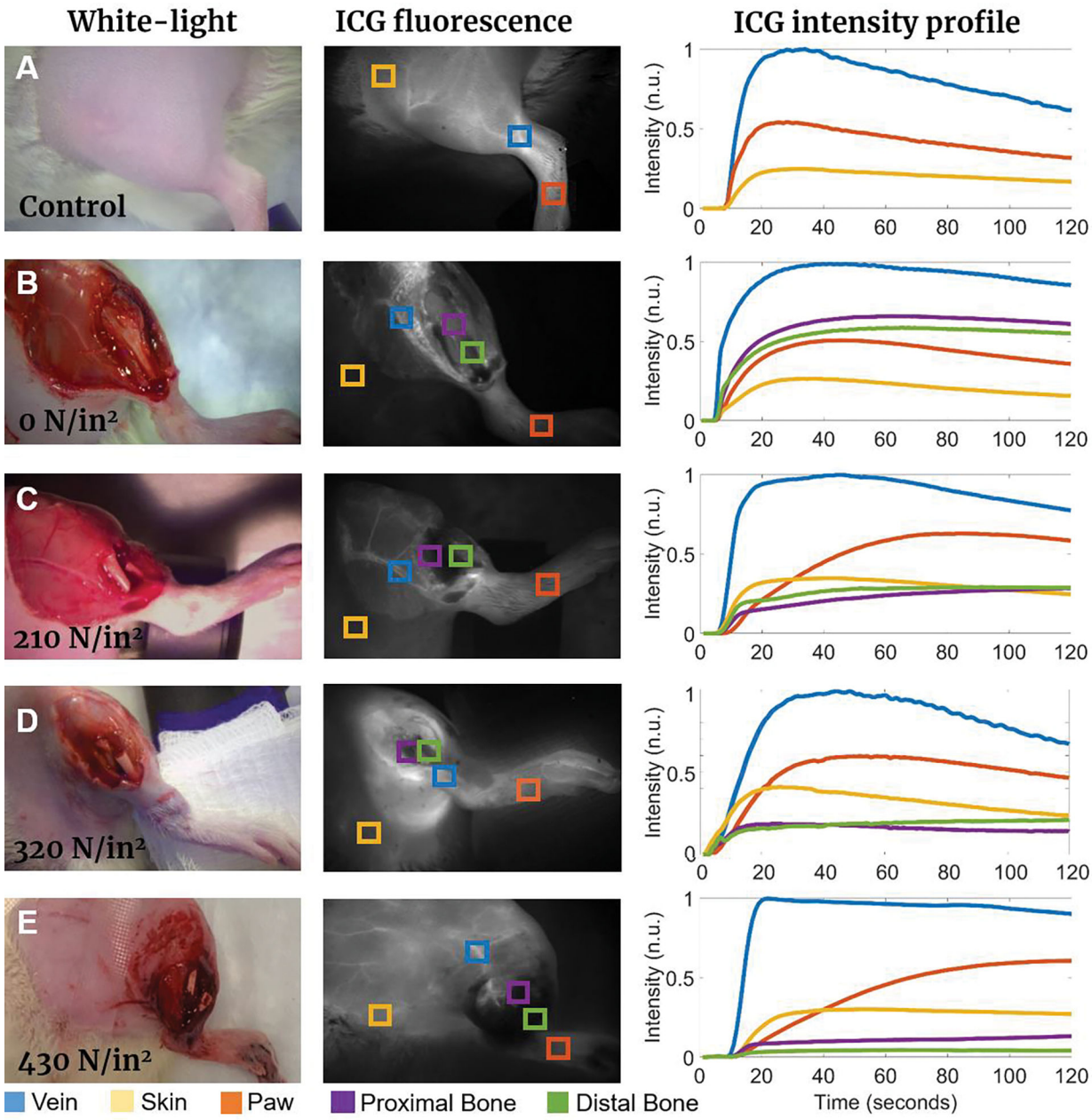

Figure 3.

Representative white light images, ICG fluorescence intensity images, and corresponding fluorescence intensity profiles for 210–430 N/in^2 impact force conditions: **(a)** Control case where no trauma or skin incision was performed; **(b)** 0 N/in^2 case where no trauma was inflicted but tibia was surgically exposed for baseline proximal and distal bone perfusion evaluation; **(c)** Minimum impact (210 N/in^2, grade I injury); **(d)** Medium impact (320 N/in^2, grade II injury); **(e)** Severe impact (430 N/in^2, grade III injury). Intensity profiles (curve colors match the corresponding ROI squares in ICG fluorescence images) indicate changes in the characteristic intensity curves for each ROI over time.

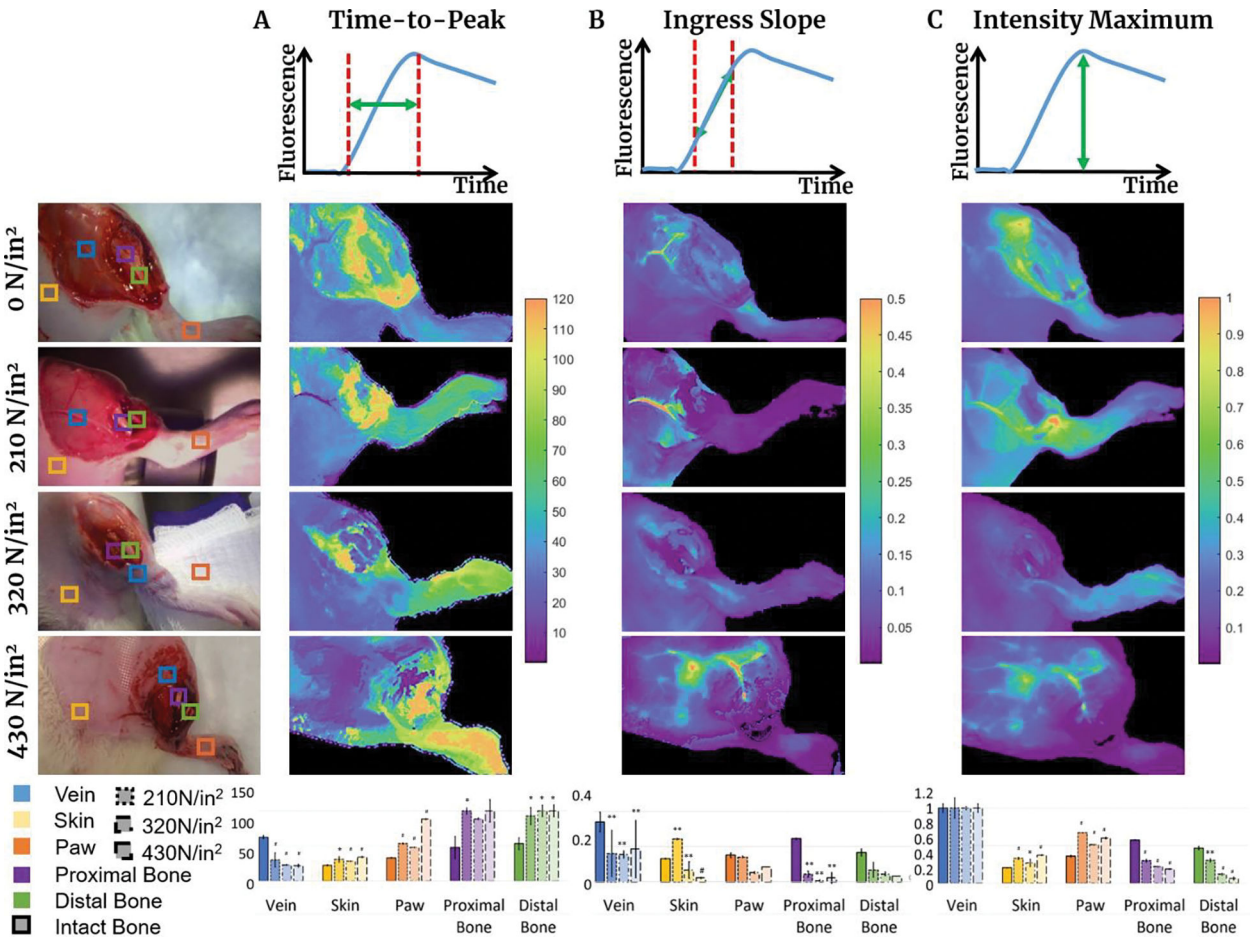

Figure 4.

Characteristic properties of fluorescence intensity profiles compared for each trauma level and ROI: **(a)** Time-to-peak (TTP) visualization, perfusion map for each trauma case, and ROI comparison bar graph. TTP defined by the time from 2% of maximum intensity to maximum intensity; **(b)** Ingress slope (IS) visualization, perfusion map for each trauma case, and ROI comparison bar graph. IS describes initial slope of the intensity profile defined between 25% of I_{max} and 75% of I_{max}; **(c)** Maximum Intensity (I_{max}) visualization, perfusion map for each trauma case, and ROI comparison graph. I_{max} described by point at which maximum fluorescence intensity is detected. It is normalized to the maximum intensity of the femoral vein ROI for each trauma case. * $p < 0.05$, ** $p < 0.01$, # $p < 0.001$.

Table 1.

Category distributions of fracture and soft tissue injury in groups in live rats.

Rat No.	Force, N/in^2	Gustilo Grade	Observed damage to:			
			Skin	*Vasculature*	*Muscle*	*Bone*
1	210	I	X*	-	-	X
2		I	X*	-	-	X
3		I	X*	-	-	X
4	320	II	X	-	X	X
5		IIIa/b	X	-	X	X
6		II	-	X	X	X
7	430	IIIc	X	X	X	X
8		IIIc	X	X	X	X
9		IIIc	X	X	X	X

*Small poke hole created, consistent with Gustilo type I injuries